OPEN ACCESS



Shocks Power Tidal Disruption Events

Taeho Ryu^{1,2}, Julian Krolik², Tsvi Piran³, Scott C. Noble⁴, and Mark Avara^{5,6}

Max Planck Institute for Astrophysics, Karl-Schwarzschild-Strasse 1, D-85748 Garching, Germany; tryu@mpa-garching.mpg.de

Physics and Astronomy Department, Johns Hopkins University, Baltimore, MD 21218, USA

Recail Institute of Physics, Hebrew University, Jerusalem 91904, Israel

Gravitational Astrophysics Laboratory, NASA Goddard Space Flight Center, Greenbelt, MD 20771, USA

Institute of Astronomy, University of Cambridge, Madingley Road, Cambridge CB3 0HA, UK

Center for Computational Relativity and Gravitation, Rochester Institute of Technology, Rochester, NY 14623, USA

Received 2023 May 8; revised 2023 August 22; accepted 2023 August 30; published 2023 October 20

Abstract

Accretion of debris seems to be the natural mechanism to power the radiation emitted during a tidal disruption event (TDE), in which a supermassive black hole tears apart a star. However, this requires the prompt formation of a compact accretion disk. Here, using a fully relativistic global simulation for the long-term evolution of debris in a TDE with realistic initial conditions, we show that at most a tiny fraction of the bound mass enters such a disk on the timescale of observed flares. To "circularize" most of the bound mass entails an increase in the binding energy of that mass by a factor of \sim 30; we find at most an order-unity change. Our simulation suggests it would take a timescale comparable to a few tens of the characteristic mass fallback time to dissipate enough energy for "circularization." Instead, the bound debris forms an extended eccentric accretion flow with eccentricity \simeq 0.4–0.5 by \sim two fallback times. Although the energy dissipated in shocks in this large-scale flow is much smaller than the "circularization" energy, it matches the observed radiated energy very well. Nonetheless, the impact of shocks is not strong enough to unbind initially bound debris into an outflow.

Unified Astronomy Thesaurus concepts: Black hole physics (159); Galaxy nuclei (609); Gravitation (661); Hydrodynamics (1963); Stellar dynamics (1596)

1. Introduction

A tidal disruption event (TDE) takes place when a star that has wandered into the vicinity of a supermassive black hole (SMBH) is torn apart by the SMBH's gravitational field. About half of the stellar mass is left unbound and is ejected to infinity, while the other (bound) half returns to the vicinity of the BH. The end result is a flare of optical/UV, X-ray, and, at times, radio emission.

During the last decades, TDEs have transformed from a theoretical prediction (Hills 1988; Rees 1988) to an observational reality (Gezari 2021). With the use of numerous detectors, ranging from ROSAT (and now eROSITA) in X-rays to GALEX in the UV, and multiple telescopes in the optical band, including systematic surveys like the Sloan Digital Sky Survey (Blanton et al. 2017), ASAS-SN (Shappee et al. 2014), Pan-STARRS (Kaiser et al. 2002), and, more recently, the Zwicky Transient Facility (Bellm et al. 2019), more than a hundred TDEs have now been detected. Upcoming observations with the Rubin Observatory will provide an overwhelming amount of data in the near future.

Although TDEs are of great interest in their own right, their properties offer a wide range of opportunities to learn about other astrophysical questions. They can reveal quiescent SMBHs and possibly permit inference of their masses. They present otherwise unobtainable information about nonsteady accretion onto SMBHs and the conditions for jet launching. In addition, understanding the rates of TDEs would reveal

Original content from this work may be used under the terms of the Creative Commons Attribution 4.0 licence. Any further distribution of this work must maintain attribution to the author(s) and the title of the work, journal citation and DOI.

valuable information concerning the stellar dynamics in galaxy cores.

Early theoretical predictions pointed out that the bound debris returns to the BH at a rate $\propto t^{-5/3}$ (Rees 1988; Phinney 1989). It was then speculated that, having returned, matter quickly forms a disk whose outer radius is comparable in size to the pericenter of the star's original trajectory. With such a small scale, the inflow time through the disk should be so short that the light emitted by the disk would follow the matter fallback, i.e., likewise at a rate $\propto t^{-5/3}$. With a characteristic temperature $\sim 10^5 - 10^6$ K, the emitted light would be in the far-UV/EUV or soft X-ray band, and the peak luminosity would be much larger than Eddington.

However, the observed luminosity rarely reaches the Eddington luminosity for the expected SMBH masses. In addition, when more TDEs were discovered in the optical, it was realized that typical temperatures are a few 10⁴ K (Gezari 2021), implying that the radiating area is much larger than that of a small disk whose radial scale is similar to the star's pericenter. Moreover, the total energy radiated during the flare period is generally 2 orders of magnitude smaller than the energy expected if half the stellar mass had been efficiently accreted onto an SMBH. In fact, it is an order of magnitude smaller than the "circularization" energy that would have been emitted during the initial formation of the small disk envisioned. That the radiated energy is so small is sometimes called the "inverse energy crisis" (Piran et al. 2015; Svirski et al. 2017).

A possible explanation for the low luminosity and low temperatures observed is that the energy produced by the accretion disk is reprocessed by a radiation-driven wind ejected from the disk itself (Strubbe & Quataert 2009). If this wind carries a significant kinetic energy, it would also resolve the "inverse energy crisis" (Metzger & Stone 2016; see, however

Matsumoto & Piran 2021). An alternative possibility is that matter does not circularize quickly and most of the observed emission arises from self-intersection shocks at the apocenter (Piran et al. 2015; Shiokawa et al. 2015; Krolik et al. 2016). These shocks, which are expected to be strong at and shortly after the time of maximum mass return, take place at $\simeq O(10^3)r_{\rm g}$ from the BH ($r_{\rm g} \equiv GM_{\bullet}/c^2$ for BH mass M_{\bullet}) and are consistent with the observed luminosity, temperature, line width, and total energy generated (Ryu et al. 2020a).

The long-term fate of bound debris is less clear. Because it is created on highly eccentric orbits, with only a small further diminution in angular momentum, it may be able to fall directly into the BH, releasing very little energy (Svirski et al. 2017). Alternatively, when there has been time for the magnetorotational instability (MRI) to build strong magnetohydrodynamic (MHD) turbulence and for the gas to lose energy to radiation, the debris may accrete gradually, while radiating efficiently (Shiokawa et al. 2015).

Although it may be possible by observational means to determine whether one of these two different scenarios occurs, numerical simulations of the disruption and subsequent accretion process may provide an alternative way to resolve this issue. However, such simulations are hindered by the extreme contrasts in the length and timescales involved. Adding fully relativistic features that are critical for some of the physics ingredients also poses technical challenges.

Aiming to clarify the many questions regarding the evolution of the bound debris' energy, angular momentum, and location, in this work we present a fully relativistic numerical simulation of a complete tidal disruption of a realistic $3M_{\odot}$ star by a 10^5M_{\odot} SMBH, in which we follow the system long enough to see the majority of the bound mass return to the BH. Several of these features have never previously appeared in a global TDE simulation: a fully relativistic treatment, both in hydrodynamics and stellar self-gravity; a main-sequence internal structure for the star's initial state; and its long duration. Our simulation scheme does not include time-dependent radiation transfer; instead, we make the approximation (for our parameters, well justified for most of the debris mass) that the radiation pressure is the value achieved in LTE and does not diffuse relative to the gas.

The structure of the work is as follows: we define the physical problem and present our numerical scheme in Section 2. We discuss the results in Section 3 and their implications in Section 4. In this latter section, we also compare our results to previous work. We conclude in Section 5, where we also discuss the possible observational implications of this work.

2. The Calculation

2.1. Physics Problem

To provide a context for our choice of numerical methods and parameters, we begin with a brief discussion of our problem's overall structure. We begin with a $3\,M_\odot$ star (radius $R_\star=2.4\,R_\odot$), whose internal structure is taken from a MESA (Paxton et al. 2011) evolution to middle age on the main sequence, the age at which the hydrogen mass fraction in its core has fallen to 0.5. The star (initially placed at $r\simeq 900\,r_{\rm g}$ from the BH) approaches an SMBH of $M_\bullet=10^5\,M_\odot$ on a parabolic orbit with a pericenter distance of $r_{\rm p}\simeq 110\,r_{\rm g}$, just close enough to be fully disrupted. Although the nominal tidal

radius $r_{\rm t} = R_{\star} (M_{\bullet}/M_{\star})^{1/3}$ is $\simeq 370 \, r_{\rm g}$ for this BH mass and stellar mass, the critical distance within which a star is fully disrupted is given by $\Psi(M_{\bullet}, M_{\star})r_{\rm t}$, where the order-unity factor Ψ encodes general relativistic corrections through its M_{\bullet} dependence and stellar structure corrections through its M_{\star} dependence (Ryu et al. 2020b).

As the star passes through pericenter, it begins to be torn apart; the process is complete by the time its center of mass reaches $\sim 7500 r_{\rm g}$. During the debris' first orbit, its trajectory is ballistic, with specific orbital energy E and specific angular momentum J very close to that of the star's center of mass. Immediately after the disruption, the distribution of mass with energy dM/dE is roughly a square wave and is approximately symmetric with respect to E=0. Although order-of-magnitude arguments suggest that the half-width of the energy square wave $\Delta \varepsilon \simeq GM_{\bullet}R_{\star}/r_{\rm t}^2$, Ryu et al. (2020b) showed that this estimate should be multiplied by an order-unity correction factor $\Xi(M_{\bullet}, M_{\star})$, which depends on both M_{\bullet} and M_{\star} , as it accounts for both relativistic and stellar internal structure effects. For our parameters, $\Xi \approx 1.64$, so the energy half-width is

$$\Delta E \simeq 1.4 \times 10^{-4} c^2 \left(\frac{\Xi}{1.64}\right) \left(\frac{M_{\bullet}}{10^5 M_{\odot}}\right)^{1/3} \times \left(\frac{M_{\star}}{3 M_{\odot}}\right)^{2/3} \left(\frac{R_{\star}}{2.4 R_{\odot}}\right)^{-1}. \tag{1}$$

The semimajor axis a and the eccentricity e of the bound debris with $E=-\Delta E$ are

$$a = \frac{GM_{\bullet}}{2E} \simeq 3600 r_{\rm g} \left(\frac{\Xi}{1.64}\right)^{-1} \times \left(\frac{M_{\bullet}}{10^5 M_{\odot}}\right)^{-1/3} \left(\frac{M_{\star}}{1 M_{\odot}}\right)^{-2/3} \left(\frac{R_{\star}}{2.4 R_{\odot}}\right), \tag{2}$$

and

$$e \simeq 1 - 0.07 \left(\frac{\Xi}{1.64}\right) \left(\frac{M_{\bullet}}{10^5 M_{\odot}}\right)^{-1/3} \left(\frac{M_{\star}}{3 M_{\odot}}\right)^{1/3},$$
 (3)

respectively. The apocenter distance of the debris with $E = -\Delta E$ is then $(1 + e)a \simeq 7000r_{\rm g}$.

The bound debris, i.e., debris with E < 0, must return to the vicinity of the SMBH. The maximal mass return rate occurs when the debris with $E \simeq -\Delta E$ returns. The fallback timescale of the material with $E \simeq -\Delta E$ is very nearly its orbital period:

$$t_0 = \frac{\pi}{\sqrt{2}} \frac{GM_{\bullet}}{\Delta E^{3/2}} \simeq 7.6 \text{ days} \left(\frac{\Xi}{1.64}\right)^{-3/2} \times \left(\frac{M_{\bullet}}{10^5 M_{\odot}}\right)^{1/2} \left(\frac{M_{\star}}{3 M_{\odot}}\right)^{-1} \left(\frac{R_{\star}}{2.4 R_{\odot}}\right)^{3/2}.$$
 (4)

The maximal fallback rate is then

$$\dot{M}_0 \simeq \frac{M_{\star}}{3t_0} \simeq 0.13 \ M_{\odot} \ \text{days}^{-1} \left(\frac{\Xi}{1.64}\right)^{3/2} \times \left(\frac{M_{\star}}{10^5 \ M_{\odot}}\right)^{-1/2} \left(\frac{M_{\star}}{3 \ M_{\odot}}\right)^2 \left(\frac{R_{\star}}{2.4 \ R_{\odot}}\right)^{-3/2}.$$
 (5)

The different scales involved are why the problem is a difficult one for numerical simulation. Fluid travels through

regions where the characteristic scale on which gravity changes runs from $\sim r_{\rm g}$ to $\sim 10^4 r_{\rm g}$, while the structure of the star varies on a scale that is a fraction of $R_{\star} \sim 15 r_{\rm g}$. Similarly, the characteristic dynamical timescale ranges from $\sim r_{\rm g}$ c^{-1} to $\sim 10^6 r_{\rm g}$ c^{-1} .

2.2. Code

To treat this problem, we perform a fully relativistic global hydrodynamics simulation using a software package comprising three core codes: PATCHWORKMHD (M. Avara et al., in preparation), HARM3D (Noble et al. 2009), and a relativistic self-gravity solver (Ryu et al. 2020c).

We use the intrinsically conservative general relativistic MHD code HARM3D (Noble et al. 2009) to solve the equations of relativistic pure hydrodynamics. This code employs the Lax-Friedrichs numerical flux formula and uses a parabolic interpolation method (Colella & Woodward 1984) with a monotonized central-differenced slope limiter. Because of its robust algorithm, it has been used for studying a wide variety of SMBH accretion problems (e.g., Noble et al. 2009, 2012; Shiokawa et al. 2015; Ryu et al. 2020b, 2020c). We take radiation pressure into account by setting the pressure $p = \rho kT/\bar{m} + aT^4/3$ when the internal energy density $u = (3/2)\rho kT/\bar{m} + aT^4$. Here, ρ is the proper rest-mass density, \bar{m} is the mass per particle, and T is the temperature. We can then define an equation of state with an "effective adiabatic index" (Shiokawa et al. 2015) that varies between $\gamma = 4/3$ and 5/3, depending on the ratio of the gas pressure and radiation pressure.

Our self-gravity solver is described in detail in Ryu et al. (2020c). In brief, it constructs a metric valid in the star's center-of-mass frame by superposing the potential found by a Poisson solver operating in a tetrad frame defined at the center of mass on top of the metric for the BH's Kerr spacetime described in the center-of-mass frame. Because this is a compact freefall frame, the spacetime for the star and its close surroundings is always very nearly flat.

The large contrasts in length and timescales noted earlier make such a computation prohibitively expensive if the entire range of scales is resolved in a single domain. To overcome this difficulty, we introduce multiple domains with PATCH-WORKMHD (M. Avara et al., in preparation; first application in Avara et al. 2023). PATCHWORKMHD is an extension of the original purely hydrodynamic PATCHWORK code (Shiokawa et al. 2018) that both enables MHD and introduces a number of algorithmic optimizations. Both versions create a multiframe/ multiphysics/multiscale infrastructure in which independent programs simultaneously evolve individual patches with their own velocities, internal coordinate systems, grids, and physics repertories. The evolution of each patch is parallelized in terms of subdomains; where different patches overlap, the infrastructure coordinates boundary data exchange between the relevant processors in the different patches. A further extension of PATCHWORKMHD, specialized to problems involving numerical relativity, is described in Bowen et al. (2020).

2.3. Domain Setup

During the first part of a TDE, a star travels through extremely rarefied gas as it traverses a nearly parabolic trajectory around the BH. This situation is a prime example of the contrasts motivating our use of a multipatch system: the

characteristic lengthscales inside the star are much smaller than those in the surrounding gas; in addition, self-gravity is important inside and near the star, but not in the remainder of the volume. Consequently, during this portion of the event, we employ PATCHWORKMHD and apply it to two patches: one covering the star, the other covering the remainder of the SMBH's neighborhood. Once the star is fully disrupted, there is no further need for the star patch, and it is removed, its content interpolated onto a single remaining patch, which evolves the entire region around the SMBH.

2.3.1. The Star's Pericenter Passage—Two-patch Simulation

This first stage begins with the initial approach of the star to pericenter and ends when the star's center-of-mass trajectory reaches a distance from the SMBH $\simeq 20r_{\rm t}$. It ends here because the star is then fully disrupted. During this stage, a rectangular solid Cartesian domain denoted *Domain1* covers the volume around the star; it is completely embedded in a larger spherical coordinate domain denoted *Domain2* that ultimately covers a large spherical region centered on the SMBH.

Following the methods described in Ryu et al. (2020c), in *Domain1* we follow the hydrodynamics of gas with self-gravity in a frame that follows the star's center of mass. Initially, the domain is a cube with edge length $5R_{\star}$ and the cell size in each dimension is $\simeq R_{\star}/25$. The orientation of this box relative to the BH is rotated during the disruption in order to follow the direction of the bulk of the tidal flow, which is easily predicted from Kepler's laws. As the debris expands, the cube is adaptively extended with constant cell size to keep the debris inside the domain for as long as possible.

As the debris expands, a fraction of the debris crosses smoothly from *Domain1* to *Domain2*, where we continue to evolve it under the gravity of the SMBH without any gas self-gravity. For *Domain2*, we adopt modified spherical coordinates in Schwarzschild spacetime. That is, if the code's three spatial coordinates are (x_1, x_2, x_3) , they can represent spherical coordinates (r, θ, ϕ) through the relations

$$r = e^{x_1},$$

$$\theta = 0.5\pi \left[1.0 + h_1 x_2 + \left(1 - h_1 - \frac{2.0\theta_0}{\pi} \right) x_2^{h_2} \right],$$

$$\phi = x_3,$$
(6)

where h_1 and h_2 are tuning parameters that determine the vertical coordinate structure ($h_1 \simeq 0.03$ and $h_2 \simeq 9$) and θ_0 is the angle from the polar axis to the θ -boundaries. In this coordinate system, the radial grid cells have a constant ratio of cell dimension to radius, and the θ grid cells are concentrated near the midplane. This coordinate system is suitable for modeling systems that involve a wide range of radial scales and contain a disk-like structure near the midplane.

To be computationally efficient, instead of fixing the size and the tuning parameters throughout the simulation, we flexibly adjust the size and the resolution of *Domain2* so that it is large enough to contain the entire debris, but we do not waste cells on regions where there is no debris. This strategy reduces the computational cost by a large factor. To ensure proper resolution during the period of flexible domain size, we require at least 15–20 cells per scale height in all three dimensions. In addition, at all times during the two-patch evolution, we keep

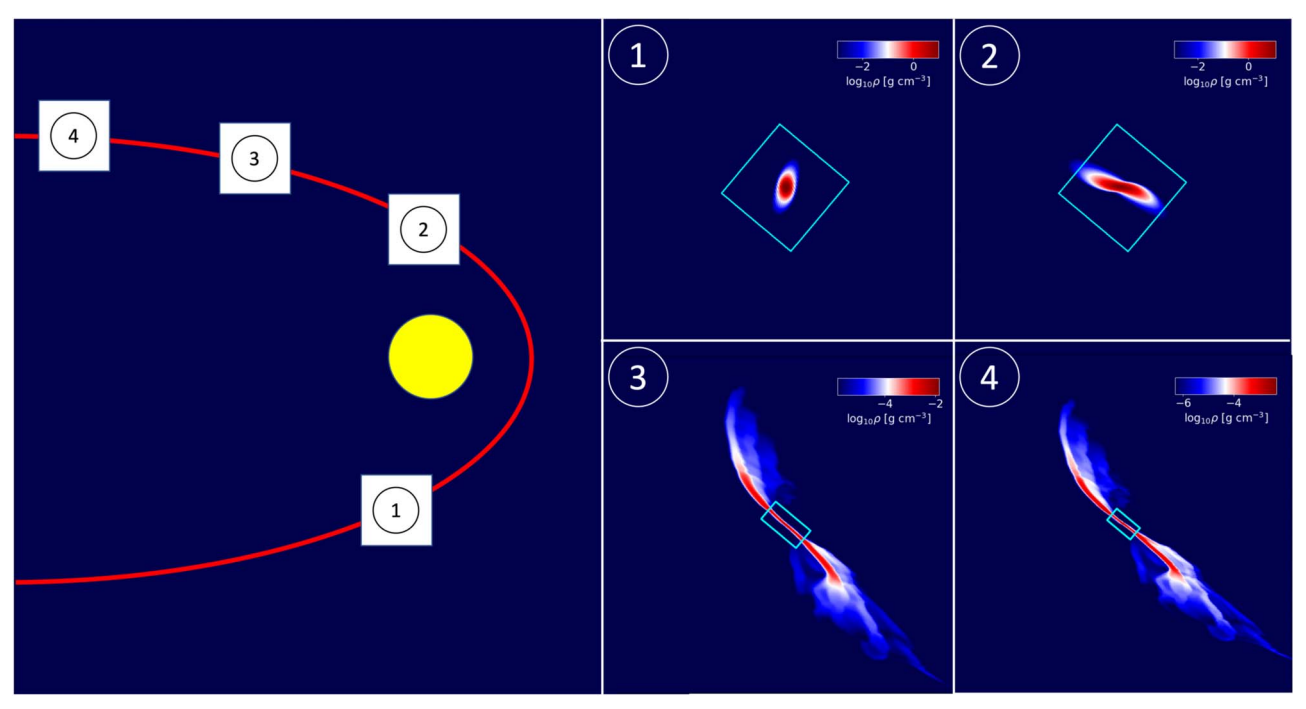


Figure 1. Successive moments in a full TDE simulated using two domains: the density distribution of the star before (1) and after (2) the pericenter passage, and the debris after the pericenter passage (3 and 4) in the equatorial plane. The yellow dot in the big left panel indicates the BH. The cyan boxes in the four right panels depict the boundary of *Domain1*. Once the star is disrupted, we increase the size of the box (from 2 to 3) to keep the debris inside *Domain1*, where the self-gravity is calculated as much as possible. The panels are not drawn to scale.

the cell sizes in the overlapping regions of both domains comparable.

At its largest extent, *Domain2* runs from $r_{\rm min}=40r_{\rm g}$ to $r_{\rm max}=18,000r_{\rm g}$. The maximum radius is chosen to be greater than the apocenter of debris that would return to the BH within a time $4t_0$; our simulation ran for $3t_0$. The minimum radius was chosen by balancing two opposing goals: minimizing the mass lost through the inner radial boundary, while maximizing the time step so as to limit computational expense. Similarly, when *Domain2* has its largest volume, the polar angle extends from $\theta_0=2^\circ$ to $\pi-\theta_0=178^\circ$. The azimuthal angle ϕ covers a full 2π when *Domain2* is largest.

We adopt outflow boundary conditions at all boundaries of *Domain2*. All the primitive variables are extrapolated to the ghost cells with zero gradients. However, to ensure outflow, if the extrapolated normal component of the fluid velocity in the ghost cells is directed inward, it is set to zero. When this domain is maximally extended azimuthally, we provide boundary conditions to the processor domains having surfaces at $\phi=0$ and $\phi=2\pi$ by matching those with the same radial and polar angle locations.

We show in Figure 1 the density distribution of the star before the pericenter passage (the top left of the four small panels), during the passage (the top right) and the debris after the passage (the bottom panels) in the equatorial plane in the two-domain simulation. The cyan box demarcates the boundary of *Domain1*. These figures demonstrate how, as the star is disrupted, the stellar debris crosses smoothly the interpatch boundary between *Domain1* and *Domain2*.

2.3.2. Single-domain Simulation

When only a tiny fraction of the star's original mass remains within *Domain1*, self-gravity becomes irrelevant (measured in the star center-of-mass frame, the acceleration throughout

Domain1 due to self-gravity is $\lesssim 10\%$ of the tidal acceleration), and gradients in gas properties are no longer connected with R_{\star} . We therefore remove *Domain1* and continue the simulation using only *Domain2*. In this stage, it takes its maximum extent.

Shocks caused by the stream–stream intersection dissipate the orbital energy into thermal energy, which results in the vertical expansion of streams. The vertical coordinate system used for the early evolution (Equation (6)) is not suitable for resolving gas at a large height, as the resolution becomes increasingly crude as z increases. To better resolve the gas at high z, we reduce the concentration of θ cells to the midplane, while leaving the r and ϕ grids untouched. To do this, we redefine $\theta(x_2)$:

$$\theta = \alpha(\tanh[b(x_2 - a)] + \tanh[b(x_2 + a)]) + 0.5\pi, \quad (7)$$

where $\alpha = -(0.5\pi - \theta_0)/[\tanh(b(-0.5 - a)) + \tanh(b(-0.5 + a))]$. Here, a and b are a set of tuning parameters that determine the vertical structure. At this stage, we fix the domain extent of r and ϕ . But we keep adjusting the domain extent and the resolution of the vertical structure flexibly, whenever it is necessary, to ensure sufficiently high vertical resolution (at least 20 cells per vertical scale height) by properly choosing the cell number (within 80-120), θ_0 ($2^\circ-15^\circ$) and the tuning parameters ($a \simeq 0.32-0.34$ and $b \sim 9.8$).

3. Results

3.1. Overview

The star becomes strongly distorted as it passes through the pericenter (see Figure 1) and then falls apart entirely as it travels farther away from the BH. When its entire mass has been dispersed, the orbital energy distribution of the debris dM/dE is not confined within the order-of-magnitude estimate of the energy distribution's width $\Delta\epsilon$; it is about twice as wide

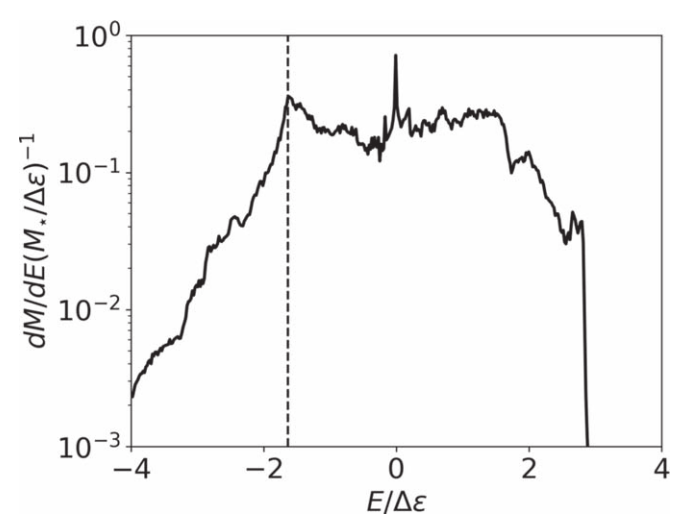


Figure 2. The energy distribution of debris at $t \simeq 0.4t_0$. The vertical dashed line $(E/\Delta\epsilon = \Xi \simeq -1.64)$ shows the characteristic energy at which the fallback rate peaks (see Figure 3).

and has extended wings (Figure 2). The mass of bound gas (E < 0) is $\simeq 0.48 M_{\star}$, slightly smaller than that of the unbound gas $(\simeq 0.52 M_{\star})$. The energy at which the peak mass return rate (Figure 3) occurs is $E \simeq -1.64 \Delta \epsilon$, or $\Xi = 1.64$. If we assume the debris follows ballistic orbits, the energy distribution presented in Figure 2 may be translated into a mass fallback rate as a function of time (Figure 3). The mass return rate peaks earlier, by a factor of $|\Xi|^{-1.5} \simeq 0.5$, than the traditional order-of-magnitude estimate predicts, and the maximal fallback rate is greater by a factor $\simeq 2.5$.

After the bound debris goes out through its orbital apocenter and returns to the region close to the BH, it undergoes multiple shocks (initially near pericenter and apocenter) and finally forms an eccentric flow, as illustrated in Figure 4 (see Section 3.3 for more details). Near pericenter, strengthening vertical gravity and orbital convergence compress the returning debris, creating a "nozzle" shock (as predicted by Evans & Kochanek 1989) visible at $t \gtrsim 0.5t_0$. Over time, the shocked gas becomes hotter and thicker. On the way to apocenter, the gas cools adiabatically. Near apocenter, the previously shocked outgoing debris collides with fresh incoming debris, creating another shock (the "apocenter" shock). Previously shocked gas close to the orbital plane is deflected inward toward the BH, while the portion farther from the plane is deflected above and below the incoming stream (see Section 3.4). These deflections broaden the angular momentum distribution. A small part of the debris loses enough angular momentum that it acquires a pericenter smaller than the star's pericenter. Other gas gains angular momentum, which results in the nozzle shock front gradually extending to larger and larger radii.

At $t \simeq (1-2)t_0$, the debris in the apocenter region undergoes a dramatic transition in shape, from well-defined incoming and outgoing streams to an extended eccentric accretion flow. By the time the return rate of the newly incoming debris declines, the mass that had arrived earlier becomes large enough to

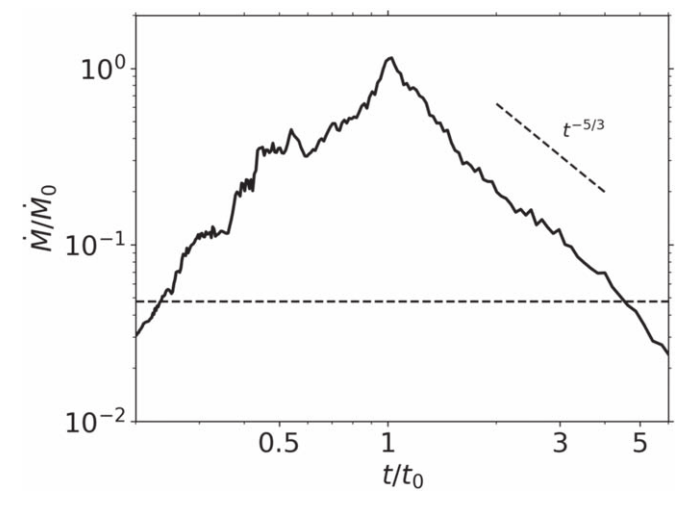


Figure 3. The mass fallback rate \dot{M} , using the energy distribution shown in Figure 2. The rate and time are normalized by $\dot{M}_0 = M_\star/3t_0$ and t_0 , respectively. The horizontal dashed line indicates the Eddington limit with radiative efficiency of 0.01 and the diagonal dashed line a power law of $t^{-5/3}$.

significantly disrupt the newly incoming debris' orbit. The space inside the apocenter region is then quickly filled with gas. The outcome is an extended eccentric accretion flow $(e \simeq 0.4-0.5 \text{ at } t \simeq 3t_0)$, most of whose mass resides at radii $\sim 10^3-10^4 r_{\rm g}$ (see Figure 5). At $t \simeq 3t_0$, only $2-3\times 10^{-2}\,M_\odot$ can be found inside $2r_{\rm p}$. By contrast, from $t\approx t_0$ onward, nearly all the thermal energy is found at small radii, a condition that has consequences for the time dependence of escaping radiation. Throughout the volume occupied by the debris, radiation pressure dominates: it is generally larger than gas pressure by a factor $\sim 10^3-10^4$.

In other words, *circularization is not prompt*: the flow retains significant eccentricity, and the great majority of the gas remains at a distance $10^3-10^4r_{\rm g}\gg r_{\rm p}$ even after several characteristic timescales. That this is so can also be seen from another point of view. At $t\simeq 3t_0$, the total amount of dissipated energy is only 10% of the energy, $E_{\rm circ}\equiv GM_{\bullet}/4r_{\rm p}$, required for the debris to fully "circularize" into a compact disk on the commonly expected radial scale of $2r_{\rm p}$. Extrapolating this slow energy dissipation rate to late times suggests that true "circularization" would take a few tens of t_0 . As we will discuss in detail in Section 4.1, the total dissipation rate is roughly constant with time from $t\simeq 0.5t_0$ until the end of our simulation at $t\simeq 3t_0$. Thus, there is no runaway increase in dissipation of the sort suggested by Steinberg & Stone (2022).

The shocked gas expands outward quasi-symmetrically (Figure 6). Because the intrinsic binding energy of the debris is much smaller than $E_{\rm circ}$, the dissipated energy is large enough to be comparable to the specific orbital energy. As a result, the expanding material is marginally bound. The radial expansion speed of the gas near the photosphere ($r \simeq 7000-10,000r_{\rm g}$; Figure 7) at $t \simeq 3t_0$ is $0.005-0.01c \simeq 1500-3000 \,{\rm km \, s^{-1}}$; the associated specific energy is $\lesssim 10^{-4}c^2$, comparable to the intrinsic energy scale, ΔE .

Although we do not incorporate radiation transfer into the simulation, we estimate the luminosity in post-processing (see Section 3.6). The bolometric luminosity rises to $(6-7)\times10^{43}\,\mathrm{erg}\,\mathrm{s}^{-1}$ in $t\simeq t_0$; its effective temperature on the photosphere is generally close to $\sim\!2\times10^5\,\mathrm{K}$.

⁷ The density fluctuations visible in newly returning matter are likely numerical artifacts; they are erased by the first shock the gas encounters and have no subsequent influence.

⁸ We ignore here the effect of recombination, as this energy is negligible compared with the orbital energy: even at apocenter, the ratio of gas kinetic energy to recombination energy is $\sim (GM_*/R_*)/E_{\rm recomb} \sim O(100)$.

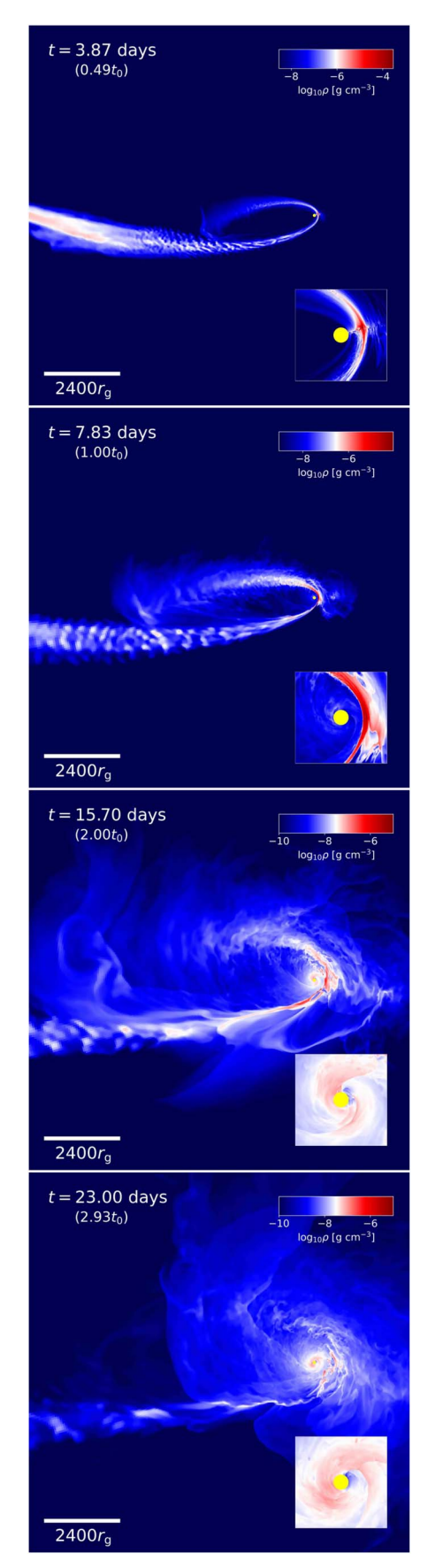


Figure 4. The density distribution around the BH excision (yellow dot) in the equatorial plane at four different times, $t/t_0 = 0.5$, 1, 2, and 3. The extent of the inset is $500r_g$.

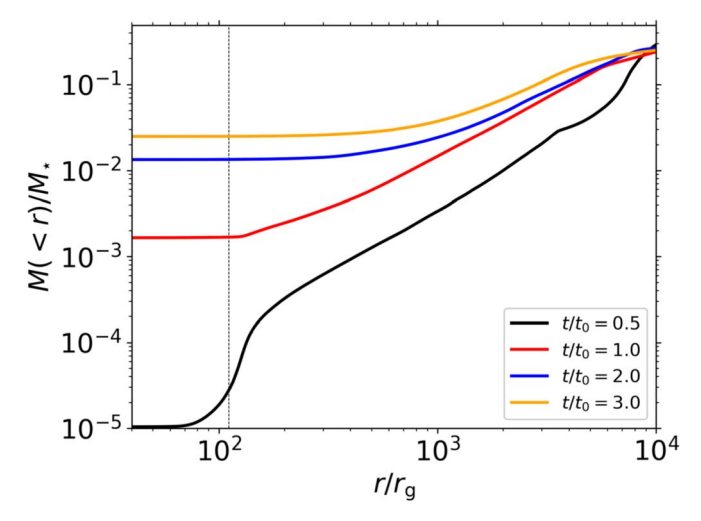


Figure 5. Accumulated mass normalized by M_{\star} as a function of the distance from the SMBH at $t/t_0 \simeq 0.5$, 1, 2, and 3. The dashed black vertical line indicates the pericenter distance of the original stellar orbit. The mass expelled through the radial inner boundary at $r=40r_{\rm g}$ is included as if the accreted mass is confined within $r=40r_{\rm g}$.

3.2. Formation of Shocks

It is convenient to divide the multiple shocks by approximate location: pericenter or apocenter. The compression and heating of the gas near the pericenter are depicted in detail in Figure 8. When the incoming stream is narrow and well defined (the two upper panels at $t \lesssim t_0$), the nozzle shock structure can be described in terms of two components. As the different portions of the returning stream converge, adiabatic compression raises the temperature at the center of the stream. The shock itself runs more or less radially across the stream, extending both inward and outward from the stream center. However, at later times (beginning at $t \gtrsim t_0$), the structure becomes more complex. The matter that has been deflected onto lower angular momentum orbits circulates in the region inside r_p and develops a pair of nearly stationary spiral shocks. The shock closest to the position of the nozzle shock stretches progressively farther outward, reaching $\sim 2000r_g$ by $t \simeq 2t_0$ (see Figure 4). However, while the shock extends to greater radii, it also loses strength. A similar progressive widening and weakening of the nozzle shock was found by Shiokawa et al. (2015).

Outgoing previously returned matter intersects the path of newly arriving matter in the apocenter region because a combination of apsidal rotation due to the finite duration of the disruption and relativistic apsidal precession causes earlier and later stream orbits to be misaligned (Shiokawa et al. 2015). When the apocenter shock first forms, it is relatively close to the BH ($\geq 1000r_g$), because the very first debris to return has orbital energy more negative than $-\Delta E$. As the mass return rate rises, its orbital energy also increases, so the debris apocenter moves outward. However, even at $t \simeq t_0$, when the shock is located at $r \simeq 6000r_g$, it is found closer to the BH than the apocenter distance corresponding to $E = -\Delta E$, because the outgoing stream has lost orbital energy to dissipation in the nozzle shock. At still later times, the apocenter shock moves farther inward, as the mean energy of the previously shocked matter decreases further.

Some of the outgoing material, upon collision with the incoming stream, is deflected both horizontally and vertically. In the left panel of Figure 9, we show the temperature

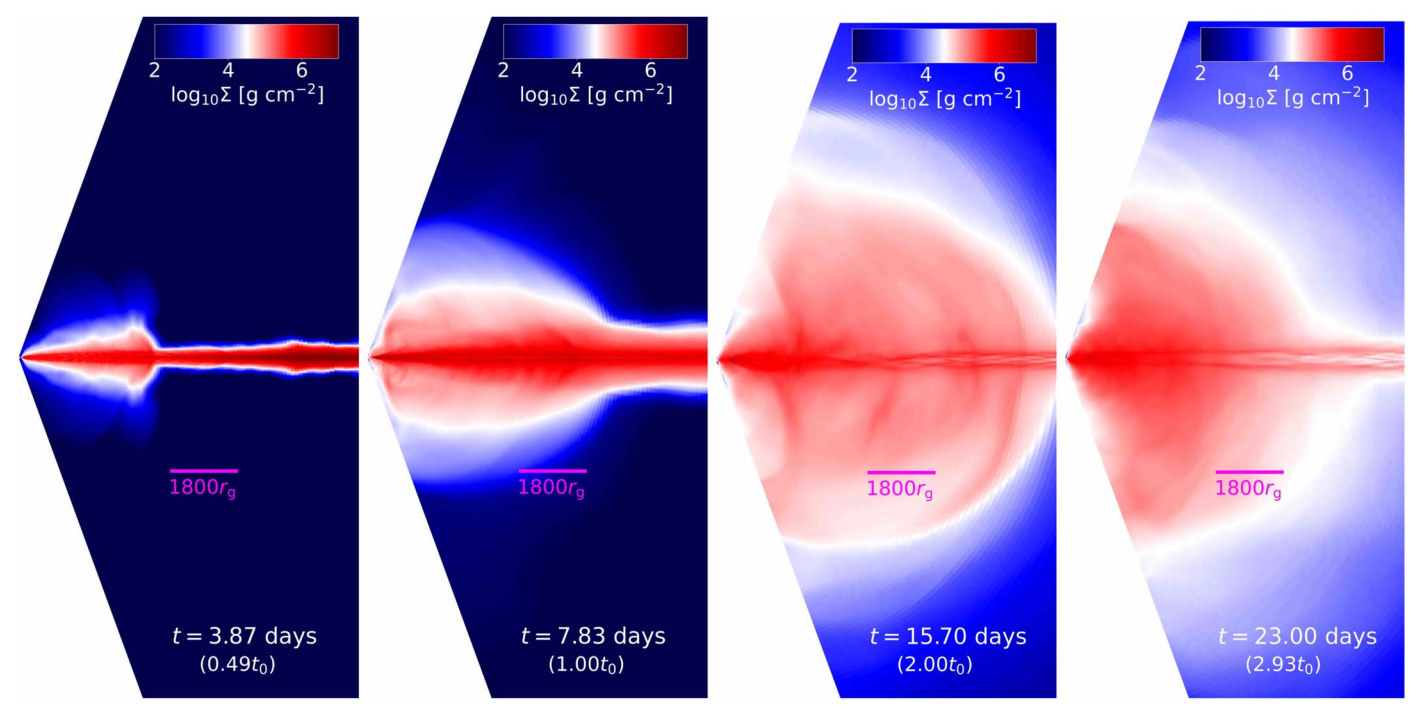


Figure 6. The azimuthally integrated density distribution at $t/t_0 = 0.5$, 1, 2, and 3.

distribution in the equatorial plane at $t \simeq t_0$. In the right panel, one can see a clear boundary between the incoming stream (with temperature $T \simeq 10^5$ K) and the outgoing stream (with $T \gtrsim 3 \times 10^5$ K). At this boundary, the outgoing stream is deflected toward the SMBH.

The two panels of Figure 9 also reveal that, just as found in Shiokawa et al. (2015), the apocenter shock splits into two (called shocks 2a and 2b by Shiokawa et al.). Shock 2a occurs where the outgoing stream encounters the incoming stream, while shock 2b (visible in these figures as the surface on which the outgoing gas temperature rises from $\simeq 3 \times 10^5$ K to $\simeq 1 \times 10^6$ K) occurs where one portion of the outgoing gas catches up with another portion that has been decelerated by gravity.

3.3. Debris Orbit Evolution

Undergoing multiple shocks, the debris becomes less eccentric and thicker both in the orbital plane and vertically. To be more quantitative, in Figure 10, we present the spherically mass-weighted averages of E/E_{circ} , angular momentum l, eccentricity e, and the aspect ratio of the debris h/r as functions of r at $t/t_0 = 0.5, 1, 2, \text{ and } 3$. At $t = 0.5t_0$, only the debris with $|E| \gtrsim 3\Delta\epsilon$ has returned or is returning, which means only a few $10^{-2} M_{\odot}$ is within $4000 r_{\rm g}$, the apocenter distance for $|E| = 3\Delta\epsilon$. At this point, the majority of the mass within $4000r_g$ is unshocked incoming debris; only the earlier returned outgoing debris has been shocked once near the pericenter. Consequently, all the mass-weighted quantities primarily reflect the properties of the newly incoming gas. The debris at $r_p \lesssim r < 4000 r_g$ has $|E| \simeq 3\Delta\epsilon \simeq 0.1 E_{\rm circ}$ and angular momentum very close to that of the original stellar orbit, giving an eccentricity of almost unity: $1 - e \lesssim 0.06$. Similarly, the aspect ratio of the debris is \approx 0.2, comparable to the value implied by $R_{\star}/r_{\rm p} \simeq 0.1$. At $0.5 \lesssim t/t_0 \lesssim 1$, the shocks begin to dissipate more energy. This results in a small fraction of the gas dropping to orbital energy $\sim -E_{\rm circ}$ and orbiting within $r_{\rm p}$. However, the global orbital properties of the debris $(r \gtrsim r_{\rm p})$ remain largely unchanged. By the second half of the simulation, enough orbital energy has been dissipated to reduce the orbital period of much of the gas by a factor of order unity (i.e., as previously noted, the dissipated energy becomes comparable to the orbital energy). The result is a structure close to virialization: the mean orbital energy as a function of radius is $\approx -GM_{\rm BH}/2r$.

A similar evolution occurs in the radial distribution of angular momentum l. Until $t \simeq t_0$, the specific angular momentum for nearly all the gas is essentially the same as that of the star. At later times, however, the shocks have greatly broadened the angular momentum distribution, and the gas has sorted itself with higher angular momentum material located at larger radii. It is, in fact, this broadening of the angular momentum distribution that leads to the outward radial extension of the nozzle shock noted in the previous subsection. The combined changes in E and l lead to a decrease in eccentricity from $\gtrsim 0.8$ –0.9 at $t \simeq t_0$ to 0.4–0.5 at $t \simeq 2t_0$. The aspect ratio changes rather little with time over the entire inner region, $r \lesssim 2000r_{\rm g}$: it rises only from $\simeq 0.2$ to $\simeq 0.5$. At larger radii, it rises from $\sim 10^{-2}$ immediately after the disruption to $\simeq 0.5$; like the inner region, this is accomplished by $t \simeq 2t_0$.

As mentioned in Section 3.1, progress toward circularization can be thought of in terms of the rate at which orbital energy is converted into thermal energy. Evaluating this rate in units of $E_{\rm circ}$ and t_0 gives a measure of the circularization "efficiency":

$$\eta \equiv \frac{|dU_{\text{gas}+\text{rad}}/dt|}{M_{\text{gas}}E_{\text{circ}}/t_0}.$$
 (8)

Here, $U_{\rm gas+rad}$ is the total thermal (gas + radiation) energy, including thermal energy that has been carried out of the simulation domain by gas flows; from $t \simeq 0.5t_0$ onward, its rate of change is roughly constant at $\simeq 1.4 \times 10^{44}$ erg s⁻¹, integrating to total thermal energy $\simeq 2.2 \times 10^{50}$ erg at the end of the simulation. $M_{\rm gas}$ is the total gas mass in the domain at

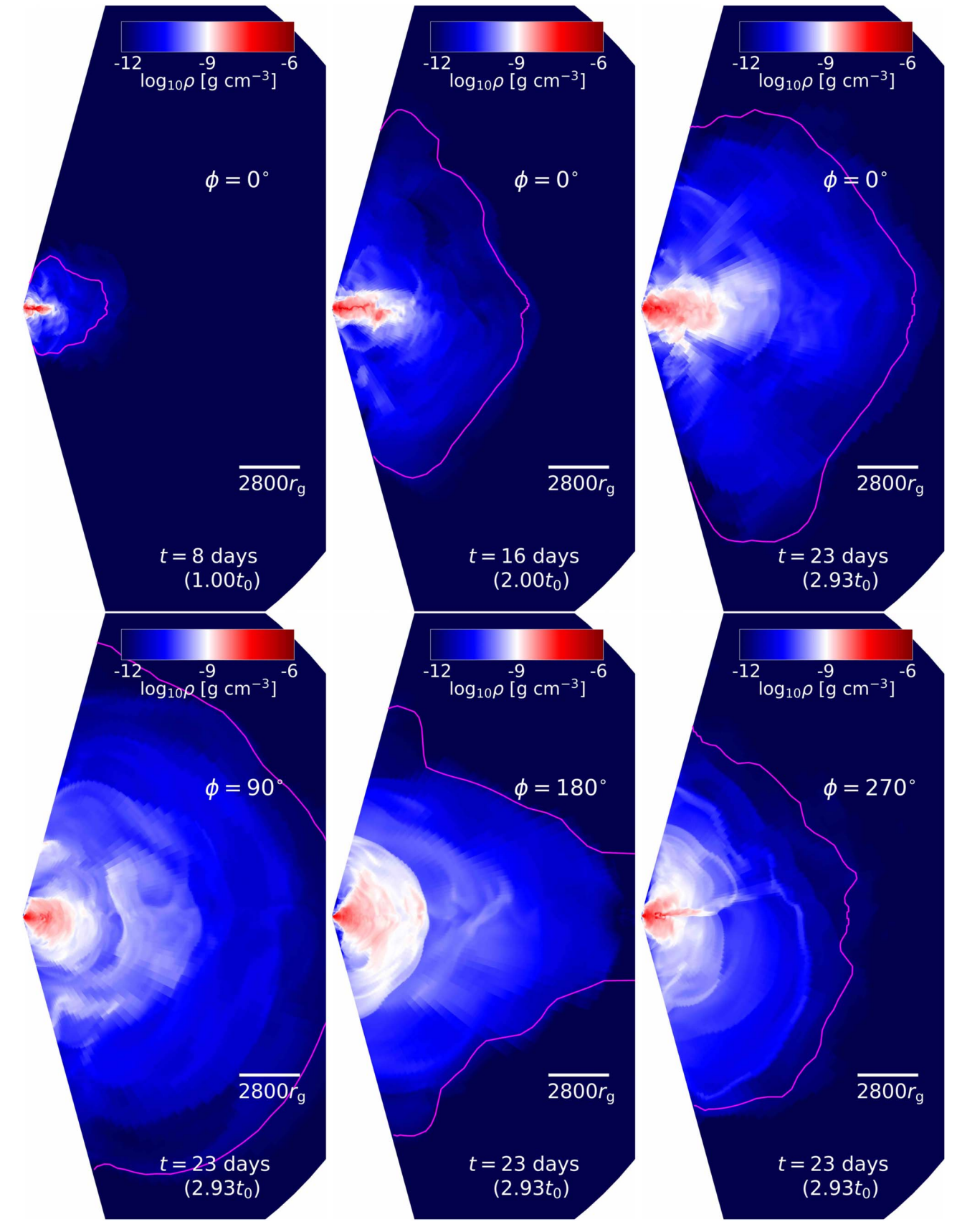


Figure 7. The location of the thermalization photosphere (magenta curves) as seen by a distant observer plotted over the density distribution at $\phi = 0$ at $t/t_0 = 1$, 2, and 3 (top panels) and at $\phi = 90^{\circ}$, 180°, and 270° at $t/t_0 = 3$ (bottom panels). We define the thermalization optical depth as $\sqrt{\tau_t \tau_{ff}}$, for τ_T (τ_{ff}) the Thomson (absorption) optical depths integrated radially inward from the outer boundary.

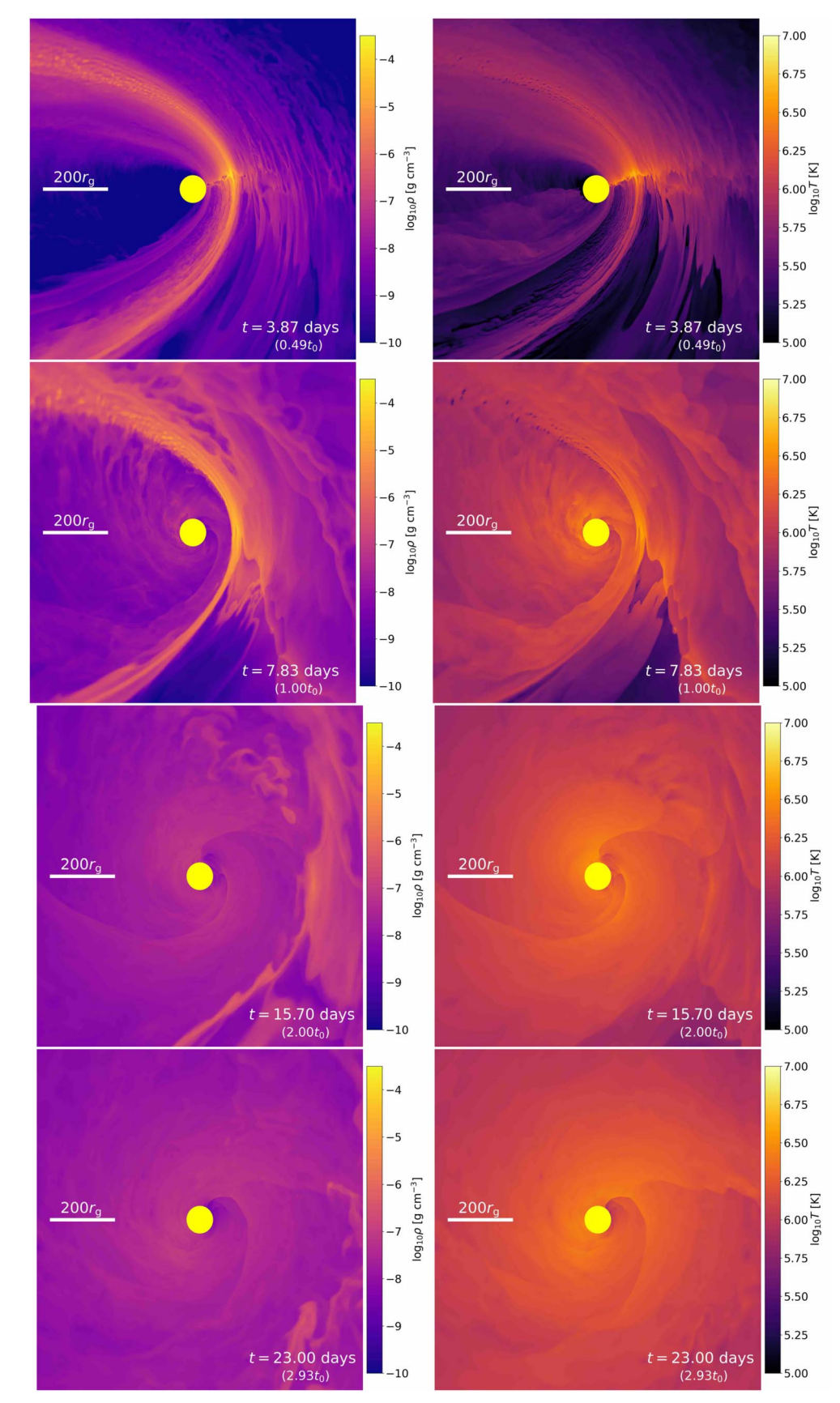


Figure 8. The density (left panels) and temperature (right panels) distribution near the BH (yellow dot) at four different times. Note the stationary spiral shock structure that appears around $2t_0$.

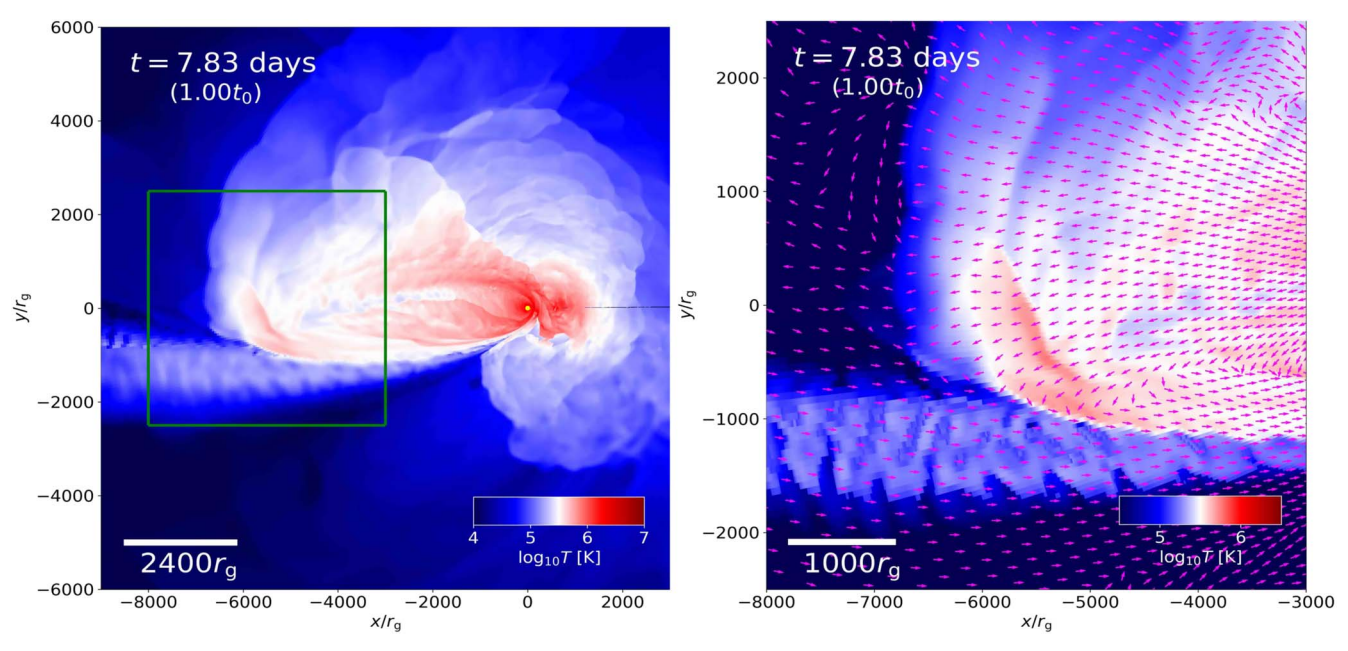


Figure 9. The temperature distribution (left) at $t = t_0$ in the equatorial plane. The right panel shows a zoom-in of the region demarcated by the green box in the left panel near where two streams collide. The arrows indicate the motion of gas. Notice the different color scales in the left and right panels.

 $r < 10^4 r_{\rm g}$. Conveniently, the mass within this region stays very nearly constant over the duration of the simulation (see the top panel of Figure 5), so the total rate of thermal energy creation is very close to directly proportional to η . This "circularization efficiency" as a function of time is shown in Figure 11.9 η rises very rapidly during the time from $t \simeq 0.5t_0$ to $t \simeq t_0$, quickly reaching a maximum ~ 0.03 . However, from $t \simeq t_0$ to the end of the simulation, its value remains very nearly flat. If it were to stay at that level until circularization was complete, the process would take $\simeq 30t_0$.

3.4. Radial Motion

The outer bound of the region in which bound debris is found expands quasi-spherically due to the combined effects of the radiation pressure gradient built by shock heating and deflection caused by stream-stream collisions. Figure 6 illustrates the azimuthally integrated density at four different times, $t/t_0 = 0.5$, 1, 2, and 3. At $t = 0.5t_0$, the outgoing gas that had been heated by the nozzle shock forms a vertically thick density structure within $3000r_g$. Later on, at $t > 0.5t_0$, the apocenter shock contributes further to the expansion of the gas. At $t \gtrsim 2t_0$, most of the mass that had been pushed outward starts to fall back toward the SMBH.

However, in the outermost $\lesssim 1\%$ of the flow, i.e., radii $7000-10,000r_g$, the gas continues moving outward with a speed of $0.005-0.01c\simeq 1500-3000~{\rm km~s}^{-1}$ even at late times. To test whether this is an incipient wind, we define unbound gas by the total energy criterion $E+E_{\rm therm}>0$, where E is the orbital (kinetic and gravitational) energy and $E_{\rm therm}$ is the thermal energy. We find almost no matter that has been made unbound after the initial disruption at any time during our simulation (i.e., up to $3t_0$). Figure 12 depicts $E+E_{\rm therm}$ at $\phi=0^\circ$ (near the nozzle shock) and 180° (near the apocenter

shock) at $t \simeq 3t_0$. As already noted, although essentially all the mass is bound, its specific binding energy is small. It is therefore not straightforward to predict the final fate of the expanding envelope based on the energy distribution measured at a specific time: energy is readily transferred from one part of the system to another, or from one form of energy to another. However, because the fallback rate declines beyond $3t_0$, the major energy source at later times would be effectively the interactions of gas in the accretion flow that has formed. Hence, the energy distribution in the outer envelope is unlikely to evolve much over time. In addition, because we allow for no radiative losses, the thermal energy content measured in the simulation data, particularly in the outer layers, is an upper bound to the actual value. This material's most likely long-term evolution is, therefore, a gradual deceleration followed by an eventual fallback.

Moving gas carries energy. Defining the mechanical luminosity by

$$L_{\rm mech}(r) = \int_{\Omega} d\Omega r^2 \rho v^r (E + E_{\rm therm}), \tag{9}$$

we find (as shown in Figure 13) that the net $L_{\rm mech}$ integrated over spherical shells is nearly always positive for $t \gtrsim t_0$ and is super-Eddington. The predominantly negative slope in $L_{\rm mech}(r)$ at $r \lesssim 10^3 r_{\rm g}$ and $r \gtrsim 5000 r_{\rm g}$ indicates that these regions are gaining energy, while the relatively constant mechanical luminosity at $10^3 r_{\rm g} \lesssim r \lesssim 5 \times 10^3 r_{\rm g}$ shows relatively insignificant energy exchange in that range of radii.

In interpreting this radial flow of mechanical luminosity, it is important to note that it is due to a mix of outwardly moving unbound matter and inwardly moving bound matter. Both signs of radial velocity are represented on almost every spherical shell; in fact, the mass-weighted mean radial velocity is generally *inward* with magnitude $\sim 300-1000 \, \mathrm{km \, s^{-1}}$. Thus, the regions gaining energy do so in large part, but not exclusively, by losing strongly bound mass.

Note that this definition of η differs from the one used by Steinberg & Stone (2022), who compare the instantaneous energy dissipation rate to the instantaneous fallback rate, $\eta' = |dU_{\rm gas+rad}/dt|(\dot{M}_{\rm fb}E_{\rm circ})^{-1}$.

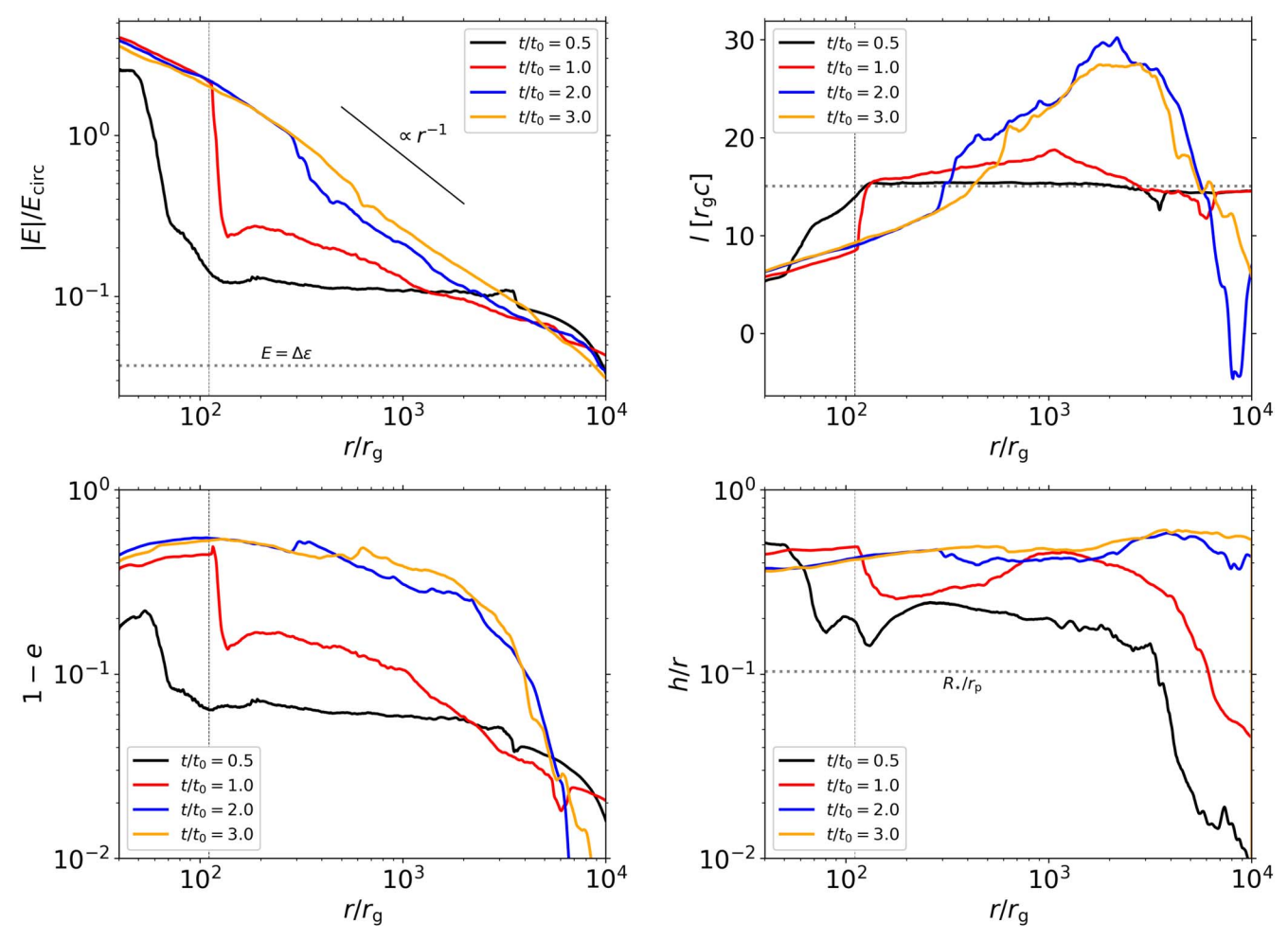


Figure 10. The mass-weighted average of the specific orbital energy of debris (top left), angular momentum (top right), eccentricity (bottom left), and aspect ratio (bottom right) for given r at $t/t_0 = 0.5$, 1, 2, and 3. The dashed gray vertical lines in all panels indicate the pericenter distance of the original stellar orbit. The dotted gray horizontal lines in some panels show different quantities: $E = \Delta \epsilon$ (top left), initial angular momentum (top right), and $R_{\star}/r_{\rm p}$ (bottom right). The diagonal black line in the top left panel shows a power law of r^{-1} .

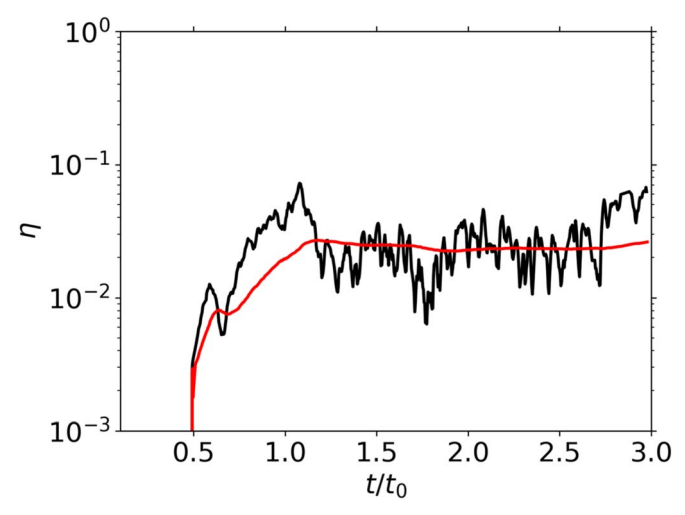


Figure 11. Circularization efficiency η , defined in Equation (8), as a function of time. The red line shows the time average of η , estimated as $\eta(t) = \int_0^t dt' \eta(t') / \int_0^t dt'$.

3.5. Matter Loss through Inner Radial Boundary

Figure 14 shows the rate at which mass falls through the inner radial boundary at $40r_{\rm g}$ and leaves the computational

domain. This rate rises rapidly from t = 0 to $t = t_0$, and from then until $t = 3t_0$ fluctuates about a nearly constant mean value $\approx 0.035 \dot{M}_0$. The total lost mass up to $t \approx 3t_0$ is $\lesssim 0.025 M_{\star}$. This is a factor ~ 3 smaller than the rate, at $t = 3t_0$, of mass loss through a similarly placed inner cutout in the simulation of Shiokawa et al. (2015).

Although the simulation provides no information about what happens to this gas after it passes within $r = 40r_g$, we can make certain informed speculations. By computing its mass-weighted mean specific energy and angular momentum, we find that its mean eccentricity is $\simeq 0.7$ –0.8 and does not evolve over time. Its mean pericenter and apocenter distances are $10 - 15r_g$ and $80-120r_{\rm g}$, respectively. These values imply that the mass lost through the boundary would not accrete onto the SMBH immediately. In fact, if it follows such an orbit, it should reemerge from the inner cutout. If it did so without suffering any dissipation, it would erase the positive energy flux we find at the inner boundary, which is due to bound matter leaving the computational domain. On the other hand, if it suffered the maximum amount of dissipation consistent with an unchanging angular momentum and settled onto circular orbits inside $40r_{o}$, it might release as much as $\simeq 10^{51}$ erg, more than enough to unbind the rest of the bound debris, whose binding energy is only ${\sim}3\times10^{50}$ erg. However, this estimate of dissipation is an

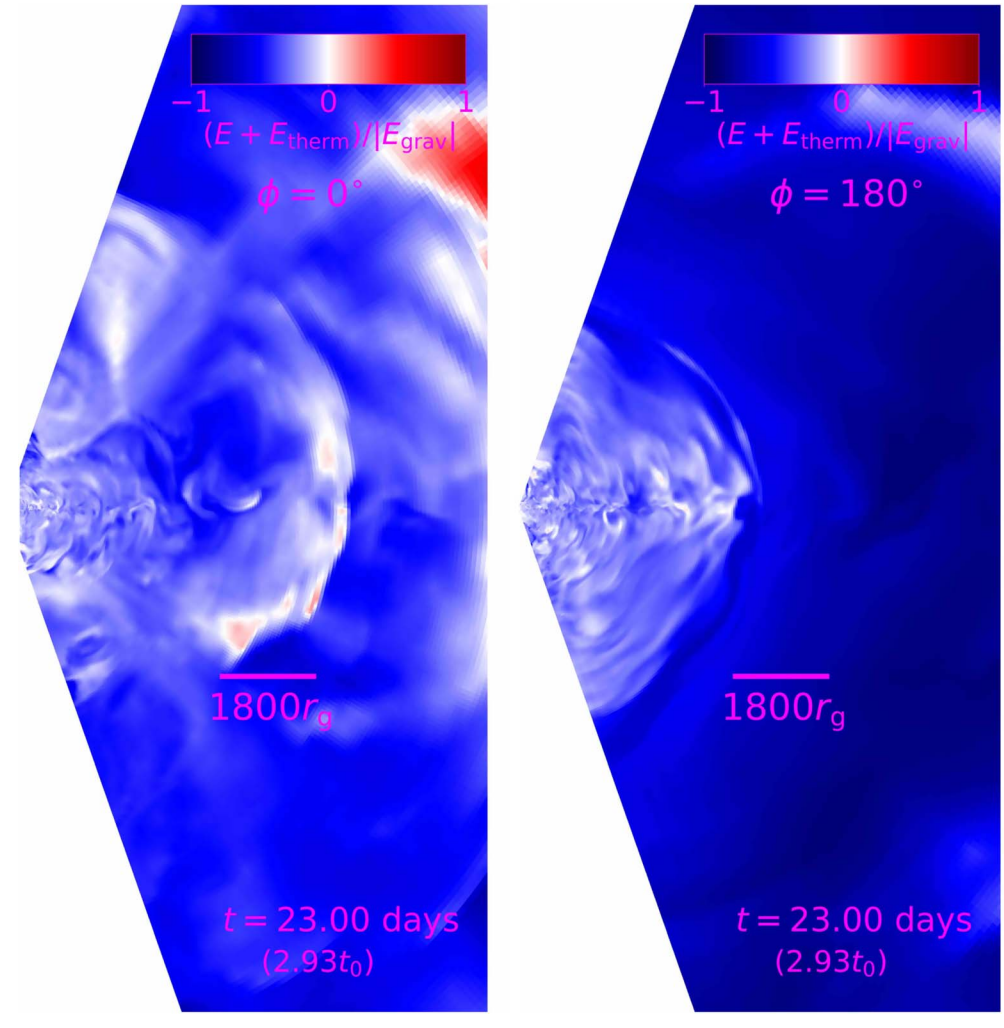


Figure 12. The distribution of the total energy $E+E_{\rm therm}$, normalized by the local gravitational potential $E_{\rm grav}=-GM_{\bullet}/r$, at $\phi=0^{\circ}$ (left, near the nozzle shock) and 180° (right, near the apocenter shock) at $t=3t_0$.

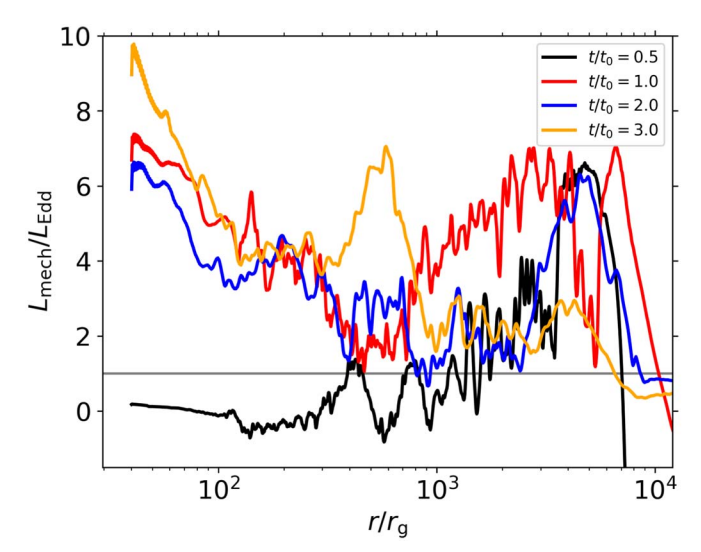


Figure 13. Radial total energy $(E + E_{\rm therm})$ flux integrated over a spherical shell at given r, normalized by the Eddington luminosity $L_{\rm Edd}$, at four different times. Positive values mean net positive (or negative) energy carried by gas moving radially outward (or inward).

upper bound, and likely a very loose one, with the actual dissipation far smaller. The locations of the shocks suffered by

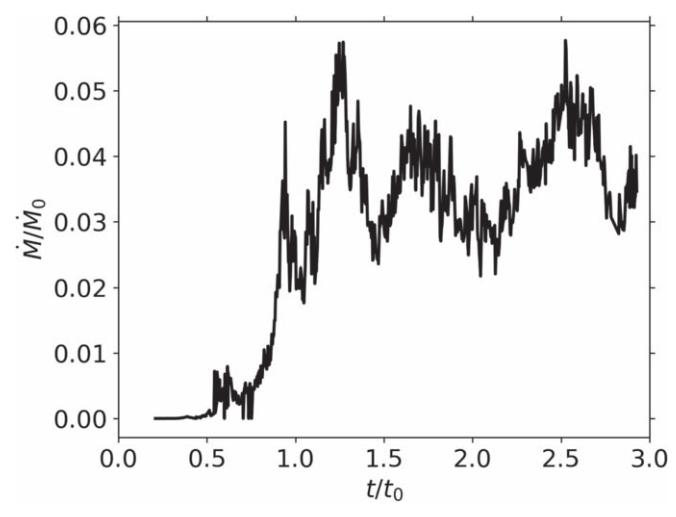


Figure 14. The rate at which gas is expelled through the inner radial boundary at $r = 40r_{\rm g}$, divided by \dot{M}_0 , as a function of t/t_0 .

this gas would be much nearer its apocenter at $\sim 100r_g$ than its pericenter, reducing the kinetic energy available for dissipation by an order of magnitude or more. Oblique shock geometry, as seen in the directly simulated shocks, sharply diminishes how

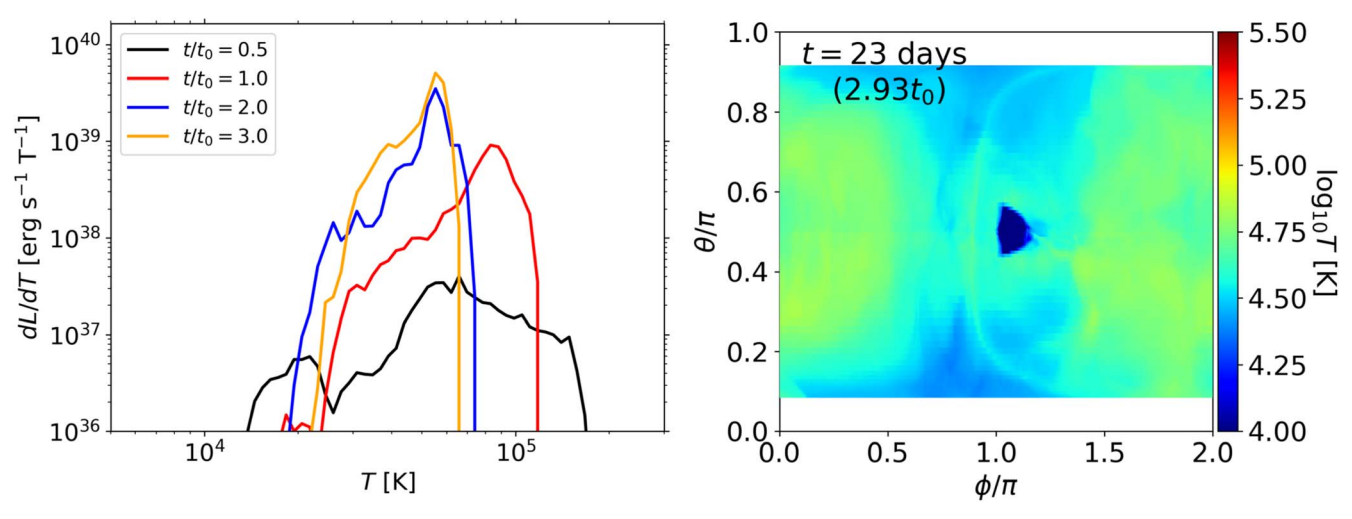


Figure 15. Left: the photosphere temperature distribution dL/dT at four different times $t/t_0 = 0.5$, 1, 2, and 3. Right: the angular distribution of the temperature at $t = 3t_0$.

much kinetic energy is dissipated per shock passage. In addition, if matter does fall onto weakly eccentric orbits with semimajor axes $<40r_{\rm g}$, it will block further inflow, thereby decreasing the net flow across the $r=40r_{\rm g}$ surface. Whatever accumulation of gas occurs within $\lesssim 100r_{\rm g}$ is also unlikely to have much effect on the bulk of the bound debris because, as is visible in Figure 8, the radial range at which the bulk of the returning gas passes through the nozzle shock moves steadily outward over time, reaching $\gtrsim 500r_{\rm g}$ by $t=3t_0$.

3.6. Radiation

To infer the bolometric luminosity of this event, we postprocess the simulation results. We first identify the thermalization photosphere with the surface where $\sqrt{\tau_{\rm T}\tau_{\rm ff}} \simeq 1$. Here, $\tau_{\rm T}$ $(\tau_{\rm ff})$ is the Thomson (absorption) optical depth integrated radially inward from the outer r boundary. The absorption cross section is calculated using an OPAL table for solar metallicity. The upper panels of Figure 7 show that the photosphere expands quasi-spherically, which is expected from the radial expansion of the outer debris. At $t = t_0$, the photosphere is quasi-spherical located at $r \simeq 4000-5000r_{\rm g}$. It expands to $9000-10,000r_{\rm g}$ at $t=2t_0$ and to $\simeq 12,000r_{\rm g}$ at $t=3t_0$. Given the eccentric orbit of debris, the radius of the photosphere depends on ϕ at a quantitative level, even while its overall shape is qualitatively round. To demonstrate the ϕ dependence, we show in the bottom panels of Figure 7 the density distribution and the photosphere at four different azimuthal angles, $\phi = 0$, 90°, 180°, and 270° at $t = 3t_0$.

We then estimate the cooling time t_{cool} at all locations inside the photosphere as

$$t_{\text{cool}}(r) = \frac{h_{\rho}\tau(r)}{c}(1 + u_{\text{gas}}/u_{\text{rad}}), \tag{10}$$

where h_{ρ} is the first-moment density scale height of the gas along a radial path, τ is the optical depth (radially integrated) to r, and $u_{\rm gas}/u_{\rm rad}$ is the ratio of the local internal energy density to the radiation energy (a ratio that is often only slightly greater than unity). We then estimate the luminosity by integrating the energy escape rate over the volume within the photosphere, but including only those locations for which $t_{\rm cool}$ is smaller than the elapsed time in the simulation. This condition accounts for the

fact that in order to leave the debris by time t, the cooling time from the light's point of origin must be less than t. The resulting expression is

$$L = \int_0^{2\pi} \int_{\theta_c}^{\pi - \theta_c} \int_{r = r(t_{\text{cool}} < t)}^{r = r(\tau = 1)} \frac{aT^4}{t_{\text{cool}}} r^2 \sin\theta dr d\theta d\phi, \tag{11}$$

where a is the radiation constant.

The local effective temperature at each individual cell near the photosphere is then calculated as $T_{\rm ph} = [(dL/dA)/\sigma]^{1/4}$, where A is the surface area of the photosphere and σ is the Stefan–Boltzmann constant. We estimate that the peak luminosity is $\simeq 10^{44}$ erg s⁻¹ $\simeq 10L_{\rm Edd}$, which occurs at $t \simeq t_0$. This is roughly the mean rate of thermal energy creation during the simulation. The photospheric temperature distribution at $t=0.5t_0$ can be described as nearly flat within the range $\times 10^4 K \lesssim T \lesssim 2 \times 10^5 K$, as shown in the left panel of Figure 15. At $t \gtrsim t_0$, the distribution becomes narrower: the distribution at $t \gtrsim 2t_0$ has a single peak at $T \simeq (5-6) \times 10^4 K$. In the right panel of Figure 15, we show the photospheric temperature distribution as a function of observer direction at $t \simeq 3t_0$. The temperature is $5-6 \times 10^4 K$ over almost the entire photosphere, except for a noticeably low-temperature spot at $\phi \simeq \pi$ and $\theta = 0.5\pi$, corresponding to the low-T incoming stream.

4. Discussion

4.1. Circularization—Fast or Slow?

The pace of "circularization" has long played a central role in understanding how TDE flares are powered. If it is rapid, i.e., takes place over a time $\lesssim t_0$, the debris joins a small $(r \lesssim r_{\rm p})$ accretion disk as soon as it first returns. In addition, accretion takes place on a short timescale compared to t_0 , because the orbital period on this scale is shorter than t_0 by a factor $(M_{\star}/M_{\star})^{1/2} \sim 10^{-3}$. Even after waiting ~ 10 orbital periods for MRI turbulence to saturate and then consuming many more orbital periods to flow inward by magnetic stresses, the total inflow is still short compared to t_0 . The dissipation rate at the time of peak mass return would then be strongly super-Eddington.

The result of our simulation, however, is that "circularization" is actually very slow. We find that the returning debris forms a large cloud that stretches all the way from the pericenter of the original stellar orbit to the apocenter of the most-bound debris, a dynamic range $\sim 30-100$. Throughout the first $3t_0$ after disruption, only a small fraction of the debris resides within the pericenter. The mass-weighted mean eccentricity falls from $\simeq 0.9$ to $\simeq 0.4-0.6$ by $t \gtrsim 2t_0$, but does not decrease further from that time to until at least $3t_0$. Thus, by this late time, the debris has neither achieved a circular orbit nor been compressed within $r \sim r_p$.

Such slow circularization is consistent with the low energy dissipation rate. The thermal energy within the system is very small compared with $E_{\rm circ}$, the energy that must be removed from the bound debris' orbital energy in order to fully circularize it. Similarly, the circularization efficiency parameter η suggests that several dozen t_0 are required in order to dissipate $E_{\rm circ}$ of the energy (see Figure 11). Thus, we may conclude that little circularization is accomplished during the time in which most of the debris mass returns to the BH.

Our conclusions on this matter agree with the earlier findings of Shiokawa et al. (2015), who used a somewhat cruder computational scheme and less realistic conditions (these authors considered a disruption of a white dwarf of $0.64 M_{\odot}$ by a BH of $500 M_{\odot}$). On the other hand, they differ with those of Steinberg & Stone (2022), who analyzed the "circularization efficiency" in terms of the heating rate per returning mass, rather than our definition, the heating rate per returned mass over a time t_0 . On the basis of tracking this definition of circularization efficiency up to $t = t_0$, they argued that it was growing exponentially on a timescale $\sim t_0$, so that full circularization might be achieved quickly. Interestingly, our definition of efficiency also grows rapidly with time during the first t_0 ; in this respect, we agree with Steinberg & Stone (2022). However, we also find that it flattens out shortly after t_0 . Thus, one possible explanation of the contrast in our conclusions about the magnitude of energy dissipation is simply that our simulation ran longer than theirs when measured in t_0 units. It is also possible that some of the differences in the results could be attributed to differences in our physical assumptions. Steinberg & Stone (2022) used a spherical harmonic oscillator potential at $r < 30 r_g$ (private conversation with Elad Steinberg) and a Paczynski-Wiita potential at larger radii, whereas we used a Schwarzschild spacetime with a cutout at $40r_g$; they described radiation transport by a flux-limited diffusion scheme, whereas we included radiation only as a contribution (often the dominant one) to the pressure. On balance, though, because the gravity descriptions used are not very different on the relevant lengthscales and the long cooling times in the system severely limit radiative diffusion, these contrasts are unlikely to explain this disagreement. Last, it is possible that the difference in parameters (our $M_{\rm BH} = 10^5 M_{\odot}$ and $M_* = 3M_{\odot}$ versus their $M_{\rm BH} = 10^6 M_{\odot}$ and $M_* = 1M_{\odot}$ may also play a role. Further simulations will be necessary in order to test this possibility.

4.2. Energy Dissipation: Shocks versus Accretion

The physical assumptions in our simulation restrict the creation of thermal energy to two mechanisms: shocks and compressive work done within the fluid. There is no energy release due to classical accretion because our equations contain neither MHD turbulence nor phenomenological viscosity. Nonetheless, we have demonstrated that shocks and compression can, without these other processes, generate enough

energy during a few t_0 to power the observed luminosity of TDEs. We estimate a photon luminosity during this period of $\sim 10^{44}$ erg s⁻¹, and all of this energy was generated by shocks and compressive work. As discussed in the previous subsection, we have demonstrated the *absence* of orbital energy loss that is a prerequisite for forming a classical accretion flow.

4.3. Outflow

A third interesting finding is that we do not find a significant unbound outflow emerging from the bound debris. Very nearly all the bound material that has returned to the vicinity of the SMBH remains bound by the end of our simulations. Although we do see outward motion, its slow speed indicates that the material remains bound (see Figure 12). It should therefore eventually slow down and fall back.

This result places an even stronger upper bound on the dissipated energy than the earlier result that there was too little dissipation to circularize the matter, as the specific energy needed to unbind the debris is significantly smaller than that needed to circularize it around the original pericenter. Whereas the circularization energy is $\sim 3 \times 10^{51}$ erg, the binding energy is only $\sim 3 \times 10^{50}$ erg. That almost no initially bound debris is rendered unbound is consistent with the observational limits on outflows from both radio and optical TDEs (Matsumoto & Piran 2021).

This conclusion, which is contrary to a number of predictions (e.g., Jiang et al. 2016; Bonnerot et al. 2021; Huang & Davis 2023), also casts some doubt on the possibility (Metzger & Stone 2016) that the kinetic energy of an outflow is the solution to the "inverse energy crisis" mentioned earlier. When the source of heating is shocks, we find negligible transport of energy to infinity associated with outflows. Interestingly, although Steinberg & Stone (2022) do find an unbound outflow, its mechanical luminosity is only $\simeq 1.6 \times 10^{42} \ {\rm erg \, s^{-1}}$ if the outflow velocity they quote, $7500 \ {\rm km \, s^{-1}}$, is its velocity at infinity. This is such a small fraction of the heating rate that even this sort of wind does not play a significant role in the energy budget. Moreover, even if all the mass lost through our inner boundary were quickly accreted in a radiatively efficient manner, as we have already estimated, the associated heat produced would be only a factor of 4-5 greater than the thermal energy generated by shocks in the first $3t_0$ after the disruption. In this sense, we have also placed a strong limit on the ability of a wind dependent upon accretion energy to carry away a large quantity of energy.

4.4. The Ultimate Fate of the Bound Debris

Our simulation ends at $3t_0$ with nearly all the bound debris $\sim 10^3 - 10^4 r_{\rm g}$ from the BH spread over a large eccentric cloud. The question naturally arises: what happens next? Extrapolating from their qualitatively similar results, Shiokawa et al. (2015) suggested that after the usual time of ~ 10 orbital periods necessary for the saturation of MHD turbulence driven by the MRI, the gas would accrete in more or less the fashion of circular accretion disks.

Since that work, it has been shown (Chan et al. 2018, 2022) that, indeed, the MRI is a genuine exponentially growing instability in eccentric disks and, in its nonlinear development, creates internal magnetic stresses comparable to those seen in circular disks. However, its outward transport of angular momentum may, in the context of eccentric disks, cause the

innermost matter to grow in eccentricity, while outer matter, the recipient of the angular momentum removed from the inner matter, becomes more circular (Chan et al. 2022).

If this is the generic result of MRI-driven turbulent stresses in an eccentric disk, accretion might be radiatively inefficient, as matter can plunge directly into the BH if it has sufficiently small angular momentum (Svirski et al. 2017). The condition for this to happen is for the angular momentum transport to be accompanied by very little orbital energy loss. It is then possible for fluid elements of very low angular momentum to fall ballistically into the SMBH after having radiated only a small amount of energy. In this case, the system will dim rapidly after the thermal energy created by shocks has diffused out in radiation.

However, it remains to be determined whether this is, in fact, the situation in TDE eccentric accretion flows. If, instead, the work done by torques associated with angular momentum transport is substantial, a compact, more nearly circular, accretion disk eventually forms. This disk will then behave much more like a conventional accretion flow, radiating soft X-rays until most of the disk mass has been consumed.

If the energy lost per unit of accreted mass comes anywhere near the $\sim\!\!0.1c^2$ of radiatively efficient accretion, the total energy radiated over this prolonged accretion phase could be quite large: $0.1 M_{\star} c^2 \approx 10^{53}$ erg. However, sufficiently long accretion timescales might keep the luminosity relatively low. There is some observational evidence for such radiation on multiyear timescales, both in X-rays (e.g., Jonker et al. 2020; Kajava et al. 2020) and UV (e.g., van Velzen et al. 2021; Hammerstein et al. 2023). In these long-term observations, the luminosity declines gradually enough $(\propto t^{-1})$ to make the total energy radiated logarithmically divergent.

A related question is posed by the matter that passed through our inner radial boundary. To the extent that some portion of it does dissipate enough energy to achieve a near-ISCO orbit, there is the possibility of significant energy release in excess of what was seen in our simulation. In fact, in order to generate soft X-ray luminosities comparable to those often seen $(\sim 10^{44} \text{ erg s}^{-1} \text{ at peak})$, all that is required is a mass accretion rate $\sim 3 \times 10^{-3} M_{\star}/t_0$. Thus, if $\sim 0.\overline{3}$ of the matter passing through our inner boundary were able to accrete onto the BH, it might be able to account for the X-ray luminosity sometimes seen, given an optically thin path to infinity. For the parameters of our simulation, there appears to be little or no solid angle through which such a path exists (see Figure 7), but, as shown by Ryu et al. (2020a), the ratio t_{cool}/t_0 falls to $\lesssim O(1)$ when $M_{\bullet} \gtrsim 10^6 M_{\odot}$. Consequently, radiative cooling might make the flow geometrically thinner for larger-M. events, permitting X-rays emitted near the center to emerge during the time of the optical/UV flare. Alternatively, for those cases that, like our simulation, have relatively long cooling times, X-ray emission may become visible only after a significant delay relative to the optical/UV light, a delay that has been observed in several TDEs (Gezari et al. 2017; Kajava et al. 2020; Hinkle et al. 2021; Goodwin et al. 2022).

4.5. Comparison with Ryu et al. (2020a)

Ryu et al. (2020a) introduced a parameter inference method TDEMASS for M_{\bullet} and M_{\star} , built on the assumption that optical TDEs are powered by the energy dissipated by the apocenter shock. In this method, one assumes that the peak luminosity and temperature occur at $t \simeq 1.5t_0$, when the most-bound debris

collide with the incoming stream at the apocenter. Using our numerical results to determine the two parameters of TDEMASS (setting c_1 , the ratio of the photospheric radius to the apocenter distance, to 1.2 and the solid angle of the photosphere to 4π), we find that the luminosity and temperature at the peak of the bolometric lightcurve would be 3×10^{44} erg s⁻¹ and 70,000 K (see Equations (1), (2), (6), and (9) of Ryu et al. 2020a).

These values can be compared with the estimates derived from our cooling time method, $L \approx 10^{44} \text{ erg s}^{-1}$ $T \approx 60,000 \text{ K}$, measured at $t \simeq 1.5t_0$. The contrast in luminosity may be a consequence of an assumption made in the method of Ryu et al. (2020a): that the heating due to shocks is radiated promptly. Although this is a reasonable approximation for $M_{\bullet} \gtrsim 10^6 M_{\odot}$, our simulation has shown that when M_{\bullet} is as small as $\sim 10^5 M_{\odot}$, cooling is significantly retarded (in fact, Ryu et al. 2020a pointed out that $t_{\text{cool}}/t_0 \propto \Xi^{5/2} \dot{M}_{\bullet}^{-7/6} M_{\star}^{4/9}$). Although our simulation suggests that this method may require some refinement in the range of small SMBH masses, overall, whether with or without the corrections suggested by the detailed numerical simulation, the peak luminosity is in the range of optical/UV-bright TDEs. The temperature estimated from the simulation is larger by only a factor of 1.2, which is reasonable given the approximate treatment of the radiation in our scheme.

5. Conclusions

Following the energy often provides a well-marked path toward understanding the major elements of a physical event. It is especially useful for TDEs, because one might define their central question as "How does matter whose initial specific orbital energy is $\sim 10^{-4}c^2$ dissipate enough energy to both power the observed radiation and then, in the long run, fall into the black hole?"

This question can be made more specific by pointing out certain milestones in energy. In a typical TDE flare, $\sim \! 3 \times 10^{50}$ erg is radiated during its brightest period, although in a number of cases an order of magnitude more is radiated over multiple-year timescales (e.g., van Velzen et al. 2021; Hammerstein et al. 2023). The immediately post-disruption binding energy of the bound gas in the simulation described here is very similar to this number, 2×10^{50} erg. The energy required to circularize all the bound gas is 1.5 dex larger, 7.5×10^{51} erg. Last, the energy that might be liberated through conventional relativistic accretion of all the bound material is $\sim \! 3\times 10^{53}$ erg.

Comparing the results of our simulation— $\sim 1.5 \times 10^{50}$ erg radiated over a time $3t_0$ long and final gas binding energy less than a factor of 2 greater than in the initial state $(3 \times 10^{50} \text{ erg})$ —to these milestones points to a number of strong implications.

First, and most importantly, the radiation we estimate as arising from our simulation is very close to the typical radiated energy during the brightest portion of the flare. In other words, the hydrodynamics we have computed, in which shocks dissipate orbital energy into heat, succeed in matching the most important quantity describing TDE flares.

Second, over this period, the binding energy of the debris does not change appreciably. It immediately follows from the virial theorem that the scale of the region occupied by the debris likewise does not change appreciably. The only modification that might be made to this conclusion is that radiation losses would increase the binding energy by a factor of $\sim 1.5-2$. The area of the photosphere is determined by the scale of the region containing the bound debris.

Third, swift "circularization," that is, confinement of the bound debris to a circular disk with outer radius $\sim r_p$, does not happen. This process requires the bulk of the debris to increase its binding energy by a factor ~ 30 ; this did not happen.

Fourth, radiatively efficient accretion of most of the debris mass onto the BH certainly did not happen. If this had occurred, the mass remaining on the grid would be substantially smaller, and the energy released would have rendered the remaining mass strongly unbound, as it corresponds to a total dissipated energy $\sim 10^3 \times \text{larger}$ than seen.

Last, we have also found that, contrary to some expectations, essentially no debris gas that was bound immediately after the disruption was rendered unbound by shock dynamics.

Acknowledgments

We are thankful to the anonymous referee for constructive comments and suggestions. We thank Elad Steinberg and Nick Stone for helpful conversations. We also thank Suvi Gezari for informing us about delayed X-ray flares in TDEs. This research project was conducted using computational resources (and/or scientific computing services) at the Advanced Research Computing at Hopkins (ARCH) core facility, supported by the National Science Foundation (NSF) grant No. OAC 1920103), the Texas Advanced Computing Center and the Max-Planck Computing & Data Facility. At TACC, we used Frontera under allocations PHY-20010 and AST-20021. In Germany, the simulations were performed on the national supercomputer Hawk at the High Performance Computing Center Stuttgart (HLRS) under the grant No. 44232. T.P. is supported by ERC grant MultiJets. J.K. is partially supported by NSF grants AST-2009260 and PHY-2110339.

Software: python (Van Rossum & Drake 2009); matplotlib (Hunter 2007); MESA (Paxton et al. 2011); HARM3D (Noble et al. 2009).

ORCID iDs

Taeho Ryu https://orcid.org/0000-0003-2012-5217
Julian Krolik https://orcid.org/0000-0002-2995-7717
Tsvi Piran https://orcid.org/0000-0002-7964-5420
Scott C. Noble https://orcid.org/0000-0003-3547-8306
Mark Avara https://orcid.org/0000-0001-9562-9677

References

```
Avara, M. J., Krolik, J. H., Campanelli, M., et al. 2023, arXiv:2305.18538
Bellm, E. C., Kulkarni, S. R., Graham, M. J., et al. 2019, PASP, 131, 018002
Blanton, M. R., Bershady, M. A., Abolfathi, B., et al. 2017, AJ, 154, 28
Bonnerot, C., Lu, W., & Hopkins, P. F. 2021, MNRAS, 504, 4885
Bowen, D. B., Avara, M., Mewes, V., et al. 2020, arXiv:2002.00088
Chan, C.-H., Krolik, J. H., & Piran, T. 2018, ApJ, 856, 12
Chan, C.-H., Piran, T., & Krolik, J. H. 2022, ApJ, 933, 81
Colella, P., & Woodward, P. R. 1984, JCoPh, 54, 174
Evans, C. R., & Kochanek, C. S. 1989, ApJL, 346, L13
Gezari, S. 2021, ARA&A, 59, 21
Gezari, S., Cenko, S. B., & Arcavi, I. 2017, ApJL, 851, L47
Goodwin, A. J., van Velzen, S., Miller-Jones, J. C. A., et al. 2022, MNRAS,
Hammerstein, E., van Velzen, S., Gezari, S., et al. 2023, ApJ, 942, 9
Hills, J. G. 1988, Natur, 331, 687
Hinkle, J. T., Holoien, T. W. S., Auchettl, K., et al. 2021, MNRAS, 500, 1673
Huang, X., Davis, S. W., & Jiang, Y.-f. 2023, ApJ, 953, 117
Hunter, J. D. 2007, CSE, 9, 90
Jiang, Y.-F., Guillochon, J., & Loeb, A. 2016, ApJ, 830, 125
Jonker, P. G., Stone, N. C., Generozov, A., van Velzen, S., & Metzger, B.
   2020, ApJ, 889, 166
Kaiser, N., Aussel, H., Burke, B. E., et al. 2002, Proc. SPIE, 4836, 154
Kajava, J. J. E., Giustini, M., Saxton, R. D., & Miniutti, G. 2020, A&A,
   639, A100
Krolik, J., Piran, T., Svirski, G., & Cheng, R. M. 2016, ApJ, 827, 127
Matsumoto, T., & Piran, T. 2021, MNRAS, 507, 4196
Metzger, B. D., & Stone, N. C. 2016, MNRAS, 461, 948
Noble, S. C., Krolik, J. H., & Hawley, J. F. 2009, ApJ, 692, 411
Noble, S. C., Mundim, B. C., Nakano, H., et al. 2012, ApJ, 755, 51
Paxton, B., Bildsten, L., Dotter, A., et al. 2011, ApJS, 192, 3
Phinney, E. S. 1989, in IAU Symp. 136, The Center of the Galaxy 136 ed.
   M. Morris (Cambridge: Cambridge Univ. Press), 543
Piran, T., Svirski, G., Krolik, J., Cheng, R. M., & Shiokawa, H. 2015, ApJ,
Rees, M. J. 1988, Natur, 333, 523
Ryu, T., Krolik, J., & Piran, T. 2020a, ApJ, 904, 73
Ryu, T., Krolik, J., Piran, T., & Noble, S. C. 2020b, ApJ, 904, 98
Ryu, T., Krolik, J., Piran, T., & Noble, S. C. 2020c, ApJ, 904, 99
Shappee, B. J., Prieto, J. L., Grupe, D., et al. 2014, ApJ, 788, 48
Shiokawa, H., Cheng, R. M., Noble, S. C., & Krolik, J. H. 2018, ApJ,
Shiokawa, H., Krolik, J. H., Cheng, R. M., Piran, T., & Noble, S. C. 2015, ApJ,
Steinberg, E., & Stone, N. C. 2022, arXiv:2206.10641
Strubbe, L. E., & Quataert, E. 2009, MNRAS, 400, 2070
Svirski, G., Piran, T., & Krolik, J. 2017, MNRAS, 467, 1426
Van Rossum, G., & Drake, F. L. 2009, Python 3 Reference Manual (Scotts
   Valley, CA: CreateSpace), https://dl.acm.org/doi/book/10.5555/1593511
van Velzen, S., Gezari, S., Hammerstein, E., et al. 2021, ApJ, 908, 4
```